Anomalous high-pressure behavior of amorphous selenium from synchrotron x-ray diffraction and microtomography

Haozhe Liu*†, Luhong Wang*, Xianghui Xiao‡, Francesco De Carlo‡, Ji Feng§, Ho-kwang Mao¶, and Russell J. Hemley†¶

*Natural Science Research Center, Academy of Fundamental and Interdisciplinary Sciences, Harbin Institute of Technology, Harbin 150080, China; ‡XOR, Advanced Photon Source, Argonne National Laboratory, Argonne, IL 60439; §Department of Chemistry and Chemical Biology, Harvard University, Cambridge, MA 02138; and ¶Geophysical Laboratory, Carnegie Institution of Washington, Washington, DC 20015

The high-pressure behavior of amorphous selenium has been investigated with time-resolved diamond anvil cell synchrotron x-ray diffraction and computed microtomography techniques. A two-step dynamic crystallization process is observed in which the monoclinic phase crystallized from the amorphous selenium and gradually converted to the trigonal phase, thereby explaining previously observed anomalous changes in electrical conductivity of the material under pressure. The crystallization of this elemental system involves local topological fluctuations and results in an unusual pressure-induced volume expansion. The metastability of the phases involved in the transition accounts for this phenomenon. The results demonstrate the use of pressure to control and directly monitor the relative densities and energetics of phases to create new phases from highly metastable states. The microtomographic technique developed here represents a method for determination of the equations of state of amorphous materials at extreme pressures and temperatures.

crystallization | volume expansion | equation of state | phase transition | metastability

The behavior of amorphous materials under pressure is a problem of great current interest. Unusual behavior, such as pressure-induced amorphization of crystalline forms, pressure-induced polyamorphism low- to high-density forms of insulating and metallic glasses, and the dynamics of pressure-induced crystallization are reported but not fully understood (1–10). The nature of the behavior of amorphous solids under pressure is complicated by their metastability and the possibility of irreversible relaxation of their properties and structure (11). Amorphous selenium (a-Se) is a model system for examining pressure effects in amorphous materials because of the wide range of structure and bonding properties expected based on the behavior of the crystalline polymorphs of the element. In experiments designed to understand the high-pressure behavior of a-Se, we have discovered an unexpected pressure-induced dynamic crystallization process associated with a volume expansion in the material. The origin of this unusual phenomenon is examined by using a microtomography technique that allows direct measurement of the equation of state (EOS) of the amorphous phase.

Recent efforts to characterize the structural evolution of group VI elements under pressure, such as novel dense chain structures in sulfur and selenium (12), and the alternating phase transition sequence in sulfur at high pressure and temperature (13), have led to a new level of understanding of the phase diagrams and structures of these materials. Under pressure, selenium exhibits a complex polymorphism, and the diversity of phases and transition sequences observed depend strongly on the starting material (12, 14–21). First studied by x-ray diffraction (XRD) in 1972 (22), a-Se was found to crystallize in a trigonal structure (t-Se) at ≈10 GPa (23–27). However, its electrical resistance was clearly different from pure t-Se in the same pressure range. Around the crystallization pressure, in situ electrical resistance measurements of a-Se showed a discontinuous drop, resulting in a resistance two to three orders of magnitude smaller than that of t-Se at the same pressure. Moreover, the electrical resistance increased unexpectedly with time when the pressure was held constant during crystallization (24, 28, 29). The discrepancy between the electrical resistance and structure of t-Se prompted further investigation into the nature of pressure-induced crystallization by using XRD techniques. With laboratory x-ray sources, exposure times per diffraction pattern for high-pressure samples varied from 100 h (22) to 24 h (25). The use of the second-generation synchrotron x-ray sources greatly reduced diffraction collection time to 10 minutes level (26, 27). It was found that the a-Se crystallized as t-Se with minor extra diffraction peaks from an unknown high-pressure phase.

Results and Discussion

We performed time-resolved XRD measurements at the 16ID-B station of the High Pressure Collaborative Access Team (HPCAT), Advanced Photon Source (APS). The high x-ray flux from this third-generation synchrotron source was essential for rapid probing of the sample in the diamond-anvil cells (DAC) in the time domain. Diffraction patterns were collected with a Mar CCD detector with exposure times of 10 s per pattern, which produced patterns of sufficiently high quality for structure refinement. Fig. 1 shows typical XRD patterns during crystallization of a-Se at 10.4 GPa and room temperature [see also supporting information (SI) Fig. S1]. Before crystallization, the XRD patterns showed only broad features indicative of fully amorphous Se (the bottom of Fig. 1). When crystallization started near 10 GPa, sharp XRD peaks appeared on top of the broad amorphous bands (Fig. 1A). The initial XRD pattern did not match t-Se, but could be indexed with a monoclinic unit cell (m-Se). Subsequently, a second XRD pattern corresponding to t-Se appeared and grew at the expense of m-Se. At the final stage of crystallization, the dominant phase was t-Se (Fig. 1F). From the in situ XRD patterns taken in short time intervals with a finely focused synchrotron x-ray beam, we can monitor the appearance and the recrystallization (competition) of these two phases in the time and spatial domain within the sample. The monoclinic phase persisted from 20 min to over hours at different locations in the sample. A pure trigonal phase could be observed at most locations ≈80 min after the start of crystalli-
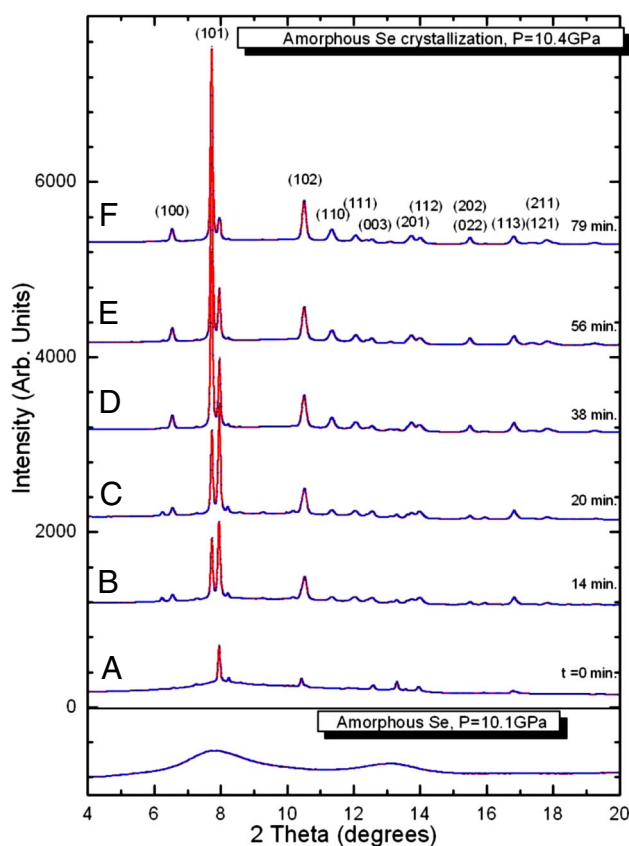

APPLIED PHYSICAL SCIENCES

Fig. 1. Typical XRD patterns during crystallization of Se at 10.4 GPa and the x-ray scattering pattern of a-Se at 10.1 GPa. The *hkl* indices based on t-Se are labeled for the top pattern. *A–F* patterns represent the various times of crystallization.

zation as shown in Fig. 2*C*. The pressure remained at 10.4 GPa during the crystallization process, indicated by the ruby pressure marker (30). Experiments were repeated by using different pressure media (methanol/ethanol/water mixture and silicone oil), and the same two-step crystallization process, and the nearly isobaric conditions were confirmed.

Using the GSAS package (31), the structure refinement of the x-ray patterns showed these two phases growing and coexisting and the *m*-Se phase disappearing (Fig. 2). The refined unit cell parameters were $a = 3.7247$ (4) Å and $c = 5.1299$ (10) Å for t-Se, and $a = 7.0432$ (19) Å, $b = 2.7815$ (9) Å, $c = 6.3306$ (20) Å, $\beta = 106.35$ (2)° for *m*-Se (Fig. 2*B*). The *m*-Se phase is similar to the monoclinic Se-II reported as a higher-pressure form of t-Se 17 GPa (24), except additional weak XRD peaks were reported in Se-II (32). This raises questions about the structural model for this phase (32). The diffraction patterns in Fig. 2 *A* and *B* agree with that of *m*-Se. First-principles calculations indicate that *m*-Se is metallic (33, 34). Its short lifetime during crystallization therefore appears to contribute to the time-dependent electrical resistance reported previously (24, 28, 29).

The density change of the material during crystallization is crucial to measure because the density of metastable *m*-Se appears ≈3.6% higher than that of t-Se based on the structure refinement (Fig. 2*B*). To measure the density of a noncrystalline material under pressure, a method was developed that uses synchrotron x-ray tomography (35). This high-pressure microtomography technique uses x-ray transparent Be gaskets and a panoramic DAC. A series of 2D radiographic images of the sample in the chamber formed by the gasket and two diamond anvils were recorded at 0.125° rotation angle *ω* increments (Fig. 3) and then reconstructed as a sequence of 3D tomographic

images (see Movie S1). Snapshots from the 3D image at selected viewing angles are shown in Fig. 4. The technique extends the range of existing high-pressure x-ray tomography methods using modified Drickamer anvil apparatus, which are limited to larger samples at lower pressures (36).

The technique allows a precise measurement of pressure–volume EOS of amorphous Se with $\Delta V / V_p$ precision 0.45% at the highest pressure conditions based on the standard error analysis detailed in *Materials and Methods* (Fig. 5*A*). *In situ* XRD was used to check the initiation of crystallization for the same sample near 10 GPa. The microtomography measurements were continued after the diffraction peaks emerged to cover the completion of the crystallization process (Fig. 1). The time dependence of the molar volume change was monitored, and volume expansion under pressure was observed to be associated with the crystallization (Fig. 5*B*). These sample volume measurement results indicate its average values, which are contributed from the time-dependent volume fraction of a-Se, *m*-Se, and t-Se in sample. At fixed high-pressure conditions, the compaction (densification) over time has been reported in the disordered systems due to relaxation; for example, the molar volume of GeO_2 glass at 7 GPa continually decreases about 1.2% over ≈100 min (37). The direct measurement of the pressure-induced volume expansion phenomenon documented here appears not to have been previously reported. The pressure in the sample chamber during the crystallization process is expected to increase because of the expansion of the sample. However, because the volume of the sample is much smaller than that of the pressure medium, and the pressure medium is more compressible than the solid sample, this pressure-shift is small. Based on the relative volumes and EOS of the sample and medium, the pressure shift is calculated to be 0.1 GPa, which is approximately the resolution of our pressure measurement, and no change in ruby signal was observed.

At ambient conditions, the densities for a-Se, t-Se, and *m*-Se are 4.280 g/cm³, 4.801 g/cm³, and 5.221 g/cm³ determined from their EOS curves at zero pressure in Fig. 5*A*. The high-density metastable phase of *m*-Se gradually converts to t-Se, which therefore has a lower internal energy despite its lower density at high pressure (Fig. 6). At ≈10 GPa, the enthalpy of *m*-Se is 0.055 eV/atom higher than that of t-Se (Fig. 6 *Inset*), which is calculated as −2.026 eV per atom, and *m*-Se is metastable relative to the trigonal phase. Thus, it gradually converts to t-Se because of its intrinsic thermodynamic stability. The anomalous volume expansion of the higher-density *m*-Se fraction to the lower-density t-Se phase is thus consistent with thermodynamics. The pressure-volume data of a-Se were fitted to a second-order Birch EOS (38). The derived bulk modulus at ambient conditions K_0 is 9.5(0.1) GPa, consistent with published data (23). The corresponding K_0 of t-Se is 14.9(0.9) GPa (21). The higher compressibility of a-Se gives density cross-over such that the density of a-Se is higher than that of t-Se at ≈10 GPa.

The pressure-induced crystallization involves nucleation and growth kinetics. Amorphous Se has branched chains that include rings of different bond lengths, and both chain and ring-type local configurations should coexist (39, 40). Theoretical calculations predict that a volume expansion occurs in the initial stages of formation of crystal nuclei (41). This suggests the appearance of crystal structures with slightly different densities. Local stresses may create a wider distribution of a variety of atomic configurations. The component of shear stress in the sample may also play, to some extent, a role in driving their metastable phase transitions, because the shear stress was found to promote the high-pressure phase transformations in nonhydrostatic conditions (42, 43) as well as in hydrostatic conditions when the shear stress is generated by the volume change of the transformation itself (44). At ≈10 GPa at room temperature, we suggest that seeds for different crystal structures are readily
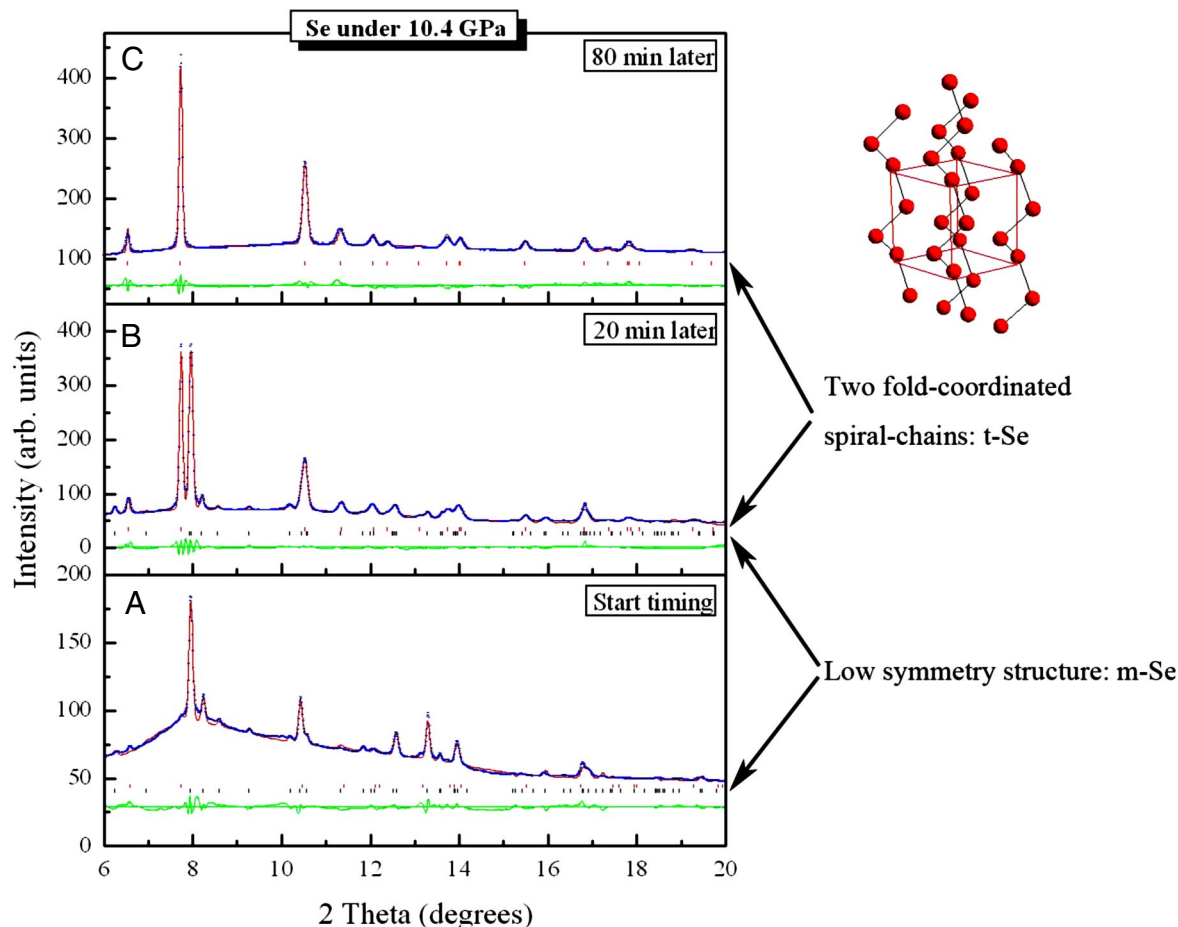
Fig. 2. X-ray diffraction structure refinements for crystallization at 10.4 GPa, in which *A*, *B*, and *C* represent the various time during crystallization. The corresponding crystal model for t-Se is illustrated.

generated because of local configuration fluctuations under stress. Some local short- and intermediate-range structures may resemble low-symmetry *m*-Se, having wide variations in bond lengths and bond angles. The greater detail of the geometrical similarity between the local structure of the a-Se and *m*-Se near crystallization pressure using the *in situ* high-energy XRD technique and the total scattering pair distribution function analysis method remains to be investigated. At the same pressure conditions, other locations in the sample may have structures close to twofold-coordinated spiral chains as in t-Se (Fig. 2). Thus, *m*-Se and t-Se could be formed at various locations based on the similarity of the local topology in a-Se. Indeed, the heterogeneous nature of the crystallization was observed in the time domain in different regions of the sample.

The pressure-induced volume expansion phenomenon documented here differs from that associated with chemical changes, for example in zeolites, which are caused by pressure-induced hydration, i.e., the sorption of water from the pressure-transmission fluid (45, 46). The process also differs from previous reports of the formation of two crystalline phases from amorphous compounds, such as chalcogenide glasses (47, 48), metallic glasses (49, 50), and polymers (51, 52). In these systems, a heterogeneous composition distribution appears to be a key factor in the nucleation and growth of two crystalline phases with changes in temperature. For example, $Ge_2Sb_2Te_5$ glass has been observed to form a metastable *fcc* $Ge_1Sb_4Te_7$ phase with increasing temperature; the appearance of the two crystal phases was attributed to local fluctuations in chemical composition (47,

48). In contrast, the crystallization we find here involves local topological fluctuations in a pure (i.e., elemental) system. The subsequent evolution with increasing pressure provides insight into pressure-induced crystallization and the effects of pressure on structural transformations of group VI elements (12, 13).

In summary, application of high-pressure synchrotron techniques has uncovered unexpected dynamics and volume expansion associated with pressure-induced crystallization of a-Se. The initial appearance of the crystal phase and the transformation between monoclinic and trigonal phases was monitored temporally and spatially. These results reveal the structural origin of the long-standing enigma of time-dependent electrical properties of the material on compression. The unusual volume expansion phenomenon under pressure associated with the "overpressurization" of a metastable phase may be more common than previously believed. Moreover, tuning relative densities and energetics of phases in this way may provide a route for creating previously undocumented structures from highly metastable states. Finally, the microtomographic technique developed here could find widespread use in accurate determinations of the EOS of glasses and melts up to megabar pressures, which is crucial to many problems in earth, planetary, and materials sciences. The results demonstrate the importance of using time- and spatially resolved high-pressure x-ray diffraction and imaging techniques to understand the kinetics of structural transformations in materials under extreme conditions.

Materials and Methods

High-Pressure XRD. The a-Se (99.99% purity) was loaded in the holes of T301 stainless steel gaskets and compressed between diamond anvils. Ruby spheres
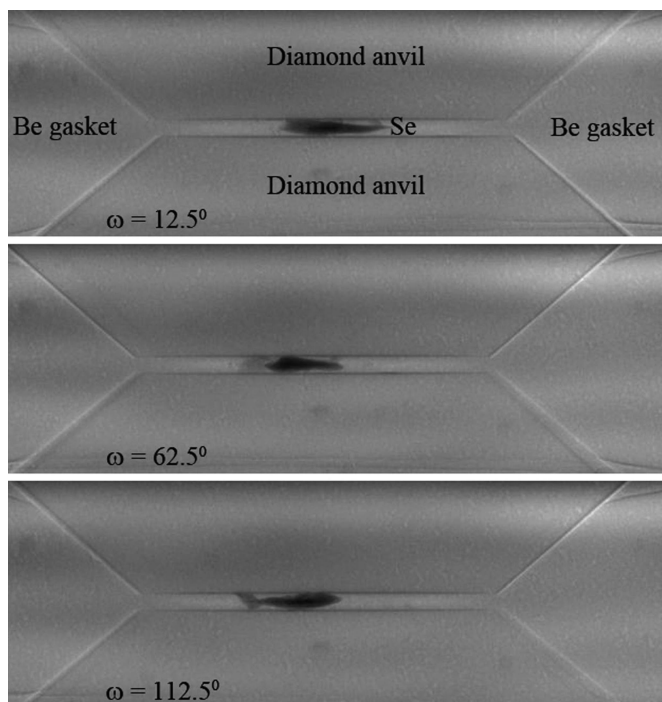
Fig. 3. Typical 2D radiographic imaging of a Se sample in a Be gasket between diamond anvils at different rotational angles.

were used as pressure markers by measurement of their fluorescence shifts (30). Monochromatic x-rays with the wavelength of 0.3682 Å were focused by a pair of K-B mirrors to a 7 μm (H) $\times$ 3 μm (V) spot onto the sample. Diffraction patterns were collected with a CCD every 10 s. Two-dimensional XRD patterns were integrated to create one-dimensional patterns by using the FIT2D program (53). Reproducibility was confirmed with multiple independent runs using methanol/ethanol (4/1) or methanol/ethanol/water mixture or silicone oil as pressure transmitting media.

High-Pressure Microtomography. The high-pressure DAC microtomography experiments were carried out at beamline 2-BM of APS. A Be gasket was used in a panoramic DAC, which provided a wide side opening. Several ruby spheres, which were used as pressure markers, were loaded together with the specimens in the sample chamber in the Be gasket. Silicone oil was used as a pressure-transmitting medium. The DAC was mounted on a rotation sample stage. The x-ray energy of 26 keV provided by a multilayer monochromator passed through the Be gasket and sample chamber to reach a CdWO$_4$ scintillator screen. A CCD camera was used to collect the radiographic images (35). Typical exposure time was 120 ms per image. The effective spatial resolution was calibrated as 1.3 μm. The limited side opening of the panoramic DAC (i.e., $\approx$138°) causes the blur on the interface between the sample and pressure medium around the related direction in the 3D reconstruction. A relative density-determination method is used to address this issue.

When x-ray illuminates a specimen, the transmission is expressed as (54)

$$I_T(s, \theta) = I_0 \cdot \exp\left[-\int_{t_1}^{t_2} \mu_\theta(s, t)dt \right] \quad \textbf{[1]}$$

where, I_0 is the illumination beam intensity, $\mu_\theta(s, t)$ is the position-dependent linear attenuation coefficient, θ is the projection angle, t is the x-ray path length in the specimen, and s is the transverse coordinate perpendicular to t. Eq. **1** can be rewritten as

$$\int_{t_1}^{t_2} \mu_\theta(s, t)dt = -\ln[I_T(s, \theta)/I_0] \quad \textbf{[2]}$$

According to the Fourier slice theorem (54), $\mu(x, y)$, which is the linear attenuation coefficient in the fixed laboratory coordinates, can be recon-
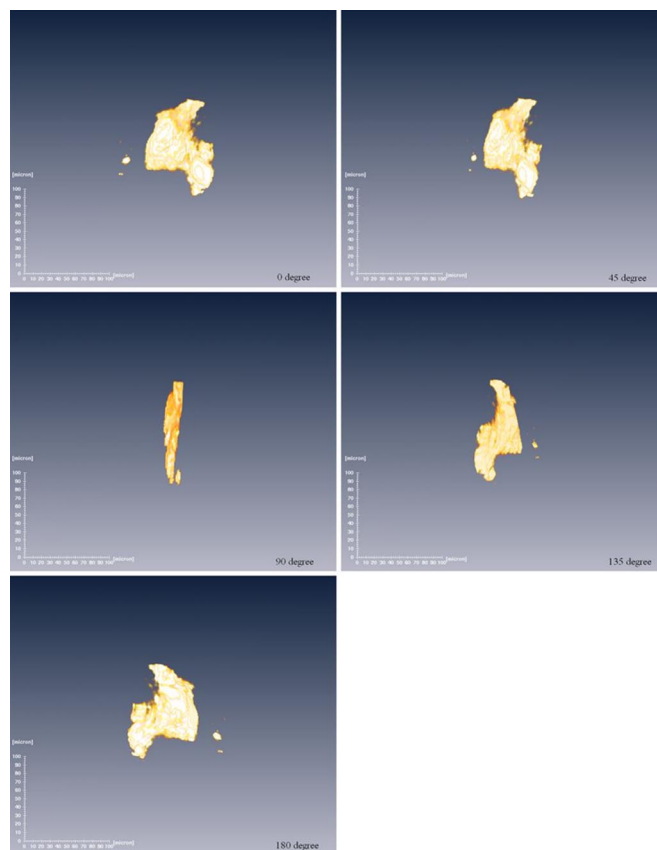

Fig. 4. Snapshot from the 3D imaging movie of a Se sample in a DAC at 10.7 GPa at various viewing angles.

structed from the series projection measurements along many view angles θ in 0–180° by the filtered-back-projection algorithm (54). $\mu(x, y)$ is proportional to the specimen mass density. After applying a constant factor, we can obtain mass density from the reconstructed $\mu(x, y)$.

In high-pressure DAC microtomography measurements, not all projections in 0–180° are available because the side opening of the panoramic DAC is <180°. However, if the specimen's density change is the same in the whole specimen along with the pressure change, the ratio between the recon-
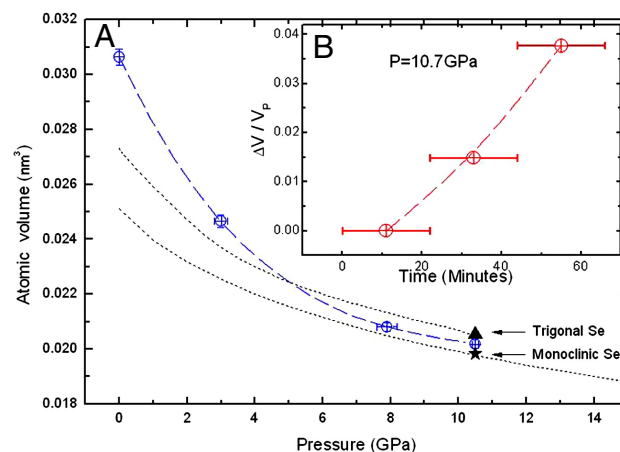

Fig. 5. Pressure-volume relations for Se. (*A*) The atomic volume change of amorphous Se under pressure determined from microtomography. For comparison, the atomic volume of t-Se and m-Se were plotted as triangle and star, respectively. The dotted lines are the experimental data for t-Se (cited from ref. 21) and first-principles calculation results for m-Se; (*B*) The time dependence of the volume change during crystallization.
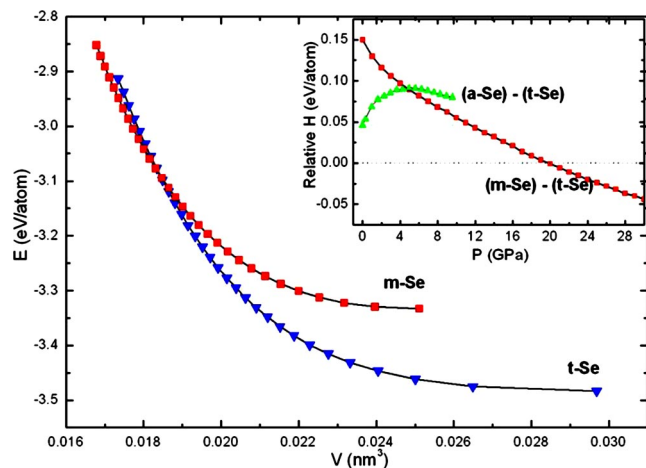
Fig. 6. The calculated total energy-volume relations of *m*-Se and t-Se. (*Inset*) The enthalpy of a-Se and *m*-Se relative to that of t-Se as a function of pressure.

structed density under one pressure condition and the reconstructed density under the reference condition should be constant over the specimen and equal to the ratio between the absolute densities under that pressure condition and the reference condition. If we further know the absolute mass density of the specimen at the reference condition ρ_0, we can calculate the absolute mass densities ρ at other pressure conditions by scaling the known density by the calculated ratios. We used this method to determine the relative density, in which the relative density values were normalized by $\rho_0 = 4.280$ g/cm^3 at ambient conditions.

The relative volume change, therefore, was calculated based on the relative density change according to

$$\frac{\Delta V}{V_P} = \frac{V - V_P}{V_P} = \frac{\rho_P}{\rho} - 1 \qquad [3]$$

The random noise in the signal includes synchrotron beam fluctuations, dark charge buildup in the CCD camera, and the efficiency of the scintillation screen and lens system during the exposure time. The corresponding white-field images were collected at every 100 sample images, which minimized the random noise effect in reconstructed density result. The standard error for relative density determination was estimated by two sets of independent measurements, and the precision is 0.45%. Similar estimation procedures were used for crystalline ZnO, Ag, and Ni samples based on their DAC mic-rotomography experimental data by comparing with their EOS (data not shown).

First-Principles Calculations. To study the EOS and enthalpies of *m*-Se and t-Se phases, total-energies are evaluated at different volume using density functional theory (DFT) within the generalized gradient approximation (55, 56). Planewave basis sets are used, as implemented in the Vienna *ab initio* Simulation Package. Perdew–Burke–Ernzerhof pseudopotentials (57) are used such that only valence electrons are included explicitly in the DFT total-energy calculations. The cutoff energy (400 eV) and k-point mesh are chosen such that a convergence of total energy is obtained within 0.1 meV per atom. The pressure and enthalpies are evaluated according to $P = -dE/dV$ and $H = E + PV$, respectively. The calculation results of total energy of *m*-Se and t-Se under pressure and enthalpy of the *m*-Se phase with reference to that of the t-Se are shown in Fig. 6. The relative enthalpy of a-Se with reference to that of t-Se were calculated according to

$$\Delta H = \int_{P_0}^{P} V dP, \qquad [4]$$

based on their P-V data as shown in Fig. 5. The crystallization enthalpy of 0.046 eV per atom at ambient conditions was used for zero pressure (58).

1. Mishima O, Calvert LD, Whalley E (1984) 'Melting ice' I at 77 K and 10 kbar: A new method of making amorphous solids. *Nature* 310:393–395.
2. Mishima O, Calvert LD, Whalley E (1985) An apparently first-order transition between two amorphous phases of ice induced by pressure. *Nature* 314:76–78.
3. Hemley RJ, Jephcoat AP, Mao HK, Ming LC, Manghnani MH (1988) Pressure-induced amorphization of crystalline silica. *Nature* 334:52–54.
4. Hemley RJ, Chen LC, Mao HK (1989) New transformations between crystalline and amorphous ice. *Nature* 338:638–640.
5. Mishima O, Takemura K, Aoki K (1991) Visual observations of the amorphous-amorphous transition in H$_2$O under pressure. *Science* 254:406–408.
6. Mishima O, Stanley HE (1998) The relationship between liquid, supercooled and glassy water. *Nature* 396:329–335.
7. Hemley RJ, Mao HK, Bell PM, Mysen BO (1986) Raman spectroscopy of SiO$_2$ glass at high pressure. *Phys Rev Lett* 57:747–750.
8. Williams Q, Jeanloz R (1988) Spectroscopic evidence for pressure-induced coordination changes in silicate glasses and melts. *Science* 239:902–905.
9. Meade C, Hemley RJ, Mao HK (1992) High-pressure x-ray diffraction of SiO$_2$ glass. *Phys Rev Lett* 69:1387–1390.
10. Sheng HW, et al. (2007) Polyamorphism in a metallic glass. *Nat Mater* 6:192–197.
11. Brazhkin VV, Lyapin AG (2003) High-pressure phase transformations in liquids and amorphous solids. *J Phys Condens Matter* 15:6059–6084.
12. Degtyareva O, et al. (2005) Novel chain structures in group VI elements. *Nat Mater* 4:152–155.
13. Grapanzano L, Crichton WA, Monaco G, Bellissent R, Mezouar M (2005) Alternating sequence of ring and chain structures in sulphur at high pressure and temperature. *Nat Mater* 4:550–552.
14. Degtyareva O, Gregoryanz E, Somayazulu M, Mao HK, Hemley RJ (2005) Crystal structure of the superconducting phases of S and Se. *Phys Rev B* 71:214104.
15. Degtyareva O, Gregoryanz E, Mao HK, Hemley RJ (2005) Crystal structure of sulfur and selenium at pressure up to 160 GPa. *High Pressure Res* 25:17–33.
16. McMahon MI, Hejny C, Loveday JS, Lundegaard LF, Hanfland M (2004) Confirmation of the incommensurate nature of Se IV at pressure below 70 GPa. *Phys Rev B* 70:054101.
17. Hejny C, McMahon MI (2004) Complex crystal structures of Te-II and Se-III at high pressure. *Phys Rev B* 70:184109.
18. Hejny C, McMahon MI (2003) Large structural modulations in incommensurate Te-III and Se-IV. *Phys Rev Lett* 91:215502.
19. Liu HZ, Jin CQ, Zhao YH (2002) Pressure induced structural transitions in nanocrystalline grained selenium. *Physica B Cond Matter* 315:210–214.
20. Akahama Y, Kobayashi M, Kawamura H (1993) Structural studies of pressure-induced phase transitions in selenium up to 150 GPa. *Phys Rev B* 47:20–26.
21. Keller R, Holzapfel WB, Schulz H (1977) Effect of pressure on the atom positions in Se and Te. *Phys Rev B* 16:4404–4412.
22. McCann DR, Cartz L (1972) High-pressure phase transformations in hexagonal and amorphous selenium. *J Chem Phys* 56:2552–2554.
23. Tanaka K (1990) Structural studies of amorphous Se under high pressure. *Phys Rev B* 42:11245–11251.
24. Ohmasa Y, Yamomoto I, Yao M, Endo H (1995) Structure and electronic properties of Te–Se mixtures under high pressure. *J Phys Soc Jpn* 64:4766–4789.
25. Bandyopadhyay AK, Ming LC (1996) Pressure-induced phase transformations in amorphous selenium by x-ray diffraction and Raman spectroscopy. *Phys Rev B* 54:12049–12056.
26. Akahama Y, Kobayashi M, Kawamura H (1997) Pressure-induced metallization and structural transition of α–monoclinic and amorphous Se. *Phys Rev B* 56:5027–5031.
27. Yang KF, et al. (2007) Pressure-induced crystallization and phase transformation of amorphous selenium: Raman spectroscopy and x-ray diffraction studies. *J Phys Condens Matter* 19:425220.
28. Aoki K, Shimomura O, Minomura S (1974) Pressure dependence of resistance and absorption edge in amorphous Se, As$_2$S$_3$, and As$_2$Se$_3$ in *Proceedings of the 4th International Confonference on High Pressure*, ed Osugi J (Kyoto University, Kyoto, Japan), pp 314–316.
29. Gupta MC, Ruoff AL (1978) Transition in amorphous selenium under high pressure. *J Apply Phys* 49:5880–5884.
30. Mao HK, Xu J, Bell PM (1986) Calibration of the ruby pressure gauge to 800 kbar under quasihydrostatic conditions. *J Geophys Res* 91:4673–4676.
31. Larson AC, Von Dreele RB (1994) General Structure Analysis System (GSAS), Los Alamos National Laboratory Report LAUR 86-748.
32. McMahon MI, Nelmes RJ (2006) High-pressure structures and phase transitions in elemental metals. *Chem Soc Rev* 35:943–963.
33. Geshi M, Oda T, Hiwatari Y (1998) High pressure phases and the structural phase transition of selenium. *J Phys Soc Jpn* 68:3141–3146.
34. Ackland GJ, Fox H (2005) Total energy calculation for high pressure selenium: The origin of incommensurate modulations in Se IV and the instability of proposed Se II. *J Phys Condens Matter* 17:1851–1859.
35. Wang YX, et al. (2001) A high-throughput x-ray microtomography system at the Advanced Photon Source. *Rev Sci Instrum* 72:2062–2068.
36. Wang YB, et al. (2005) High-pressure x-ray tomography microscope: Synchrotron computed microtomography at high pressure and temperature. *Rev Sci Instrum* 76:073709.

37. Tsiok OB, Brazhkin VV, Lyapin AG, Khvostantsev LG (1998) Logarithmic kinetics of the amorphous–amorphous transformations in SiO_2 and GeO_2 glasses under high pressure. *Phys Rev Lett* 80:999–1002.

38. Birch F (1978) Finite strain isotherm and velocities for single-crystal and polycrystalline NaCl at high pressures and 300 K. *J Geophys Res* 83:1257–1268.

39. Caprion D, Schober HR (2000) Structure and relaxation in liquid and amorphous selenium. *Phys Rev B* 62:3709–3716.

40. Nakamura K, Ikawa (2003) A medium-range order in amorphous selenium: Molecular dynamics simulations. *Phys Rev B* 67:104203.

41. Ye F, Lu K (1999) Crystallization kinetics of amorphous solids under pressure. *Phys Rev B* 60:7018–7024.

42. Wu TC, Bassett WA, Burnley PC, Weathers MS (1993) Shear-promoted phase transitions in Fe_2SiO_4 and Mg_2SiO_4 and the mechanism of deep earthquakes. *J Geophys Res* 98:19767–19776.

43. Burnley PC, Bassett WA, Wu TC (1995) Diamond anvil cell study of the transformation mechanism from the olivine to spinel phase in Co_2SiO_4, Ni_2SiO_4, and Mg_2GeO_4. *J Geophys Res* 100:17715–17723.

44. Raterron P, Chen JH, Weidner DJ (2002) A process for low-temperature olivine-spinel transition under quasi-hydrostatic stress. *Geophys Res Lett* 29:1401.

45. Lee Y, *et al.* (2002) Non-framework cation migration and irreversible pressure-induced hydration in a zeolite. *Nature* 420:485–489.

46. Lee Y, Vogt T, Hriljac JA, Parise JB, Artioli G (2002) Pressure-induced volume expansion of zeolites in the natrolite family. *J Am Chem Soc* 124:5466–5475.

47. Laine B, Trapaga G, Prokhorov E, Morales-Sánchez E, González-Hernández J (2003) Model for isothermal crystallization kinetics with metastable phase formation. *Appl Phys Lett* 83:4969–4971.

48. Prokhorov E, Trapaga G, Kovalenko YU (2006) Crystallization kinetics in materials with a two-phase formation from an amorphous phase. *J Optoelectron Adv Mater* 8:2066–2069.

49. Murty BS, Ping DH, Ohnuma M, Hono K (2001) Nanoquasicrystalline phase formation in binary Zr-Pd and Zr-Pt alloys. *Acta Mater* 49:3453–3462.

50. Louzguine DV, Inoue A (2002) Crystallization behaviour of Al-based metallic glasses below and above the glass-transition temperature. *J Non-Cryst Solids* 311:281–293.

51. Kristiansen PE, Hansen EW, Pedersen B (2001) Isothermal crystallization of polyethylene monitored by in situ NMR and analyzed within the ''Avrami'' model framework. *Polymer* 42:1969–1980.

52. Lu XF, Hay JN (2001) Isothermal crystallization kinetics and melting behaviour of poly(ethylene terephthalate). *Polymer* 42:9423–9431.

53. Hammersley AP, Svensson SO, Hanfland M, Fitch AN, Häusermann D (1996) Two-dimensional detector software: From real detector to idealised image or two-theta scan. *High Pressure Res* 14:235–248.

54. Natterer F (1986) *The Mathematics of Computerized Tomography* (B. G. Teubner, Stuttgart, and Wiley, New York).

55. Langreth DC, Perdew JP (1980) Theory of nonuniform electronic systems. I. Analysis of the gradient approximation and a generalization that works. *Phys Rev B* 21:5469–5493.

56. Langreth DC, Mehl MJ (1983) Beyond the local-density approximation in calculations of ground-state electronic properties. *Phys Rev B* 28:1809–1834.

57. Perdew JP, Burke K, Ernzerhof M (1996) Generalized gradient approximation made simple. *Phys Res Lett* 77:3865–3868.

58. Andonov P (1982) Studies of non-crystalline forms of selenium. *J Non-Cryst Solids* 47:297–339.